

PROJECTION EFFECTS OF LARGE-SCALE STRUCTURES ON WEAK-LENSING PEAK ABUNDANCES

SHUO YUAN¹, XIANGKUN LIU², CHUZHONG PAN^{3,1}, QIAO WANG⁴, ZUHUI FAN¹

¹Department of Astronomy, School of Physics, Peking University, Beijing 100871, China;
yuanshuoastro@gmail.com, fanzuhui@pku.edu.cn

²South-Western Institute for Astronomy Research, Yunnan University, Kunming 650500, China

³Center for High Energy Physics, Peking University, Beijing 100871, China

⁴Key Laboratory for Computational Astrophysics, The Partner Group of Max Planck Institute for Astrophysics, National Astronomical Observatories, Chinese Academy of Sciences, Beijing 100012, China;

ABSTRACT

High peaks in weak lensing (WL) maps originate dominantly from the lensing effects of single massive halos. Their abundance is therefore closely related to the halo mass function and thus a powerful cosmological probe. On the other hand, however, besides individual massive halos, large-scale structures (LSS) along lines of sight also contribute to the peak signals. In this paper, with ray tracing simulations, we investigate the LSS projection effects. We show that for current surveys with a large shape noise, the stochastic LSS effects are subdominant. For future WL surveys with source galaxies having a median redshift $z_{\text{med}} \sim 1$ or higher, however, they are significant. For the cosmological constraints derived from observed WL high peak counts, severe biases can occur if the LSS effects are not taken into account properly. We extend the model of [Fan et al. \(2010\)](#) by incorporating the LSS projection effects into the theoretical considerations. By comparing with simulation results, we demonstrate the good performance of the improved model and its applicability in cosmological studies.

Keywords: gravitational lensing; weak - large-scale structure of universe

1. INTRODUCTION

Being an important cosmological probe, the weak lensing (WL) effect is one of the key science drivers for a number of ongoing and future large surveys (e.g., [Albrecht et al. 2006](#); [Weinberg et al. 2013](#); [Fu & Fan 2014](#); [Kilbinger 2015](#); [LSST Dark Energy Science Collaboration 2012](#); [Amendola et al. 2013](#); [Dark Energy Survey Collaboration: Abbott et al. 2016](#)). Unlike strong lensing effects where individual lens systems can be investigated, WL analyses are statistical in nature. Therefore it is important to explore different statistics to enrich the cosmological gains from WL data.

The cosmic shear two-point (2pt) correlation/power spectrum analyses are the most widely studied ones in WL cosmology (e.g., [Kilbinger et al. 2013](#); [Becker et al. 2016](#); [Hildebrandt et al. 2017](#)). On the other hand, WL signals have reached the non-linear scales and thus the 2pt statistics cannot uncover the full cosmological information therein. The three-point correlation measurements are done for a number of surveys with the realization of much more complications, both observational and theoretical, than that of 2pt correlations ([Pen et al. 2003](#); [Semboloni et al. 2011](#); [Fu et al. 2014](#)). Con-

centrating on high signal regions, WL peak statistics has emerged as another promising means to probe non-linear structures and cosmology, complementary to cosmic shear correlation analyses ([Shan et al. 2012, 2014](#); [X. K. Liu et al. 2015b](#); [J. Liu et al. 2015a](#); [Kacprzak et al. 2016](#); [Martinet et al. 2018](#); [Shan et al. 2018](#)).

WL peaks, particularly high peaks, arise primarily from the lensing effects of massive halos along their lines of sight ([White et al. 2002](#); [Hamana et al. 2004](#); [Dietrich & Hartlap 2010](#); [Fan et al. 2010](#); [Yang et al. 2011](#); [Lin & Kilbinger 2015](#); [Shirasaki et al. 2015](#)). The high peak abundance is thus a reflection of the halo mass function, and a sensitive cosmological probe considering further the cosmology-dependent lensing kernel. It is less affected by baryonic physics than normal cluster abundances where certain baryonic observable-mass relations are needed. However, apart from massive halos, other effects can also impact the peak signals, notably the projection effect of large-scale structures (LSS) and the shape noise resulting from the intrinsic ellipticities of source galaxies ([Tang & Fan 2005](#); [Fan et al. 2010](#); [Yang et al. 2011](#); [Hamana et al. 2012](#); [Liu & Haiman 2016](#)). To predict accurately the WL peak abundance for cosmological studies, we should take them into ac-

count carefully.

In principle, numerical simulations can include various effects, and we can build empirical templates of peak counts for different cosmological models incorporating different observational effects with respect to specific surveys (Dietrich & Hartlap 2010). By comparing with observational peak counts, we therefore are able to derive cosmological constraints (J. Liu et al. 2015a; Kacprzak et al. 2016).

Such an approach is numerically intensive noting the high dimensions of the cosmological parameter space and different astrophysical and observational effects. Thus theoretical models are highly desirable for performing cosmological studies efficiently. Furthermore, the physical picture related to WL peaks can be seen more clearly in theoretical models which need to specify different effects explicitly (Marian et al. 2009; Maturi et al. 2010; Hamana et al. 2012; Lin & Kilbinger 2015; Shirasaki et al. 2015).

In Fan et al. (2010) (here after, F10) the WL high peak abundance is modeled by assuming that the true WL peaks are from the lensing effects of individual massive halos. In addition, the shape noise effect is carefully included, which not only generates false peaks but also influences the peak signals from halos. The comparison with simulations shows that the model works very well in the case of surveys with the source galaxies having a shallow redshift $z \sim 0.7$, a number density $n_g \sim 10 \text{ arcmin}^{-2}$ and a survey area $\sim 150 \text{ deg}^2$. For such surveys, the projection effect of LSS is minor comparing to the shape noise. This model has been applied in the cosmological studies by analyzing WL peak counts using data from KiDS survey (Shan et al. 2018), CFHTLenS survey (X. K. Liu et al. 2016) and CFHT Stripe 82 survey (Shan et al. 2014; X. K. Liu et al. 2015b).

For the ongoing and upcoming surveys, the survey depth can be improved considerably to detect more far-away galaxies for WL analyses. This will result in a suppression of the shape noise as well as a growth of the LSS projection effects. In such cases, the LSS effects must be included in the theoretical modelling carefully. In addition, the sky coverage will be enlarged by orders of magnitude and the statistical errors of WL peak counts will expectedly decrease. Therefore even in the case that the LSS projection effect is minor, it is still necessary to consider this effect for accurate modelling.

Recently, the comparisons between WL peak counts from a large set of simulations and from the halo-based Monte Carlo model named CAMELUS (Lin & Kilbinger 2015) are shown in Zorrilla Matilla et al. (2016). It is found that for high peaks, CAMELUS works well for

the source galaxies at $z_s = 1$ and with the cosmological parameters Ω_m and σ_8 close to the current best values, where Ω_m and σ_8 are the dimensionless matter density of the universe at present and the linear extrapolated density perturbations smoothed over a top-hat scale of $8.0 h^{-1} \text{ Mpc}$, respectively. For higher values e.g., $\Omega_m \sim 0.5$ and $\sigma_8 \sim 0.9$, the deviations between the results from simulations and those from CAMELUS are shown up. We note that for high peaks, CAMELUS is essentially the same as that of F10 and it does not include the LSS contributions beyond halos. For high Ω_m and σ_8 , we expect stronger LSS projection effects than those of low Ω_m and σ_8 . This should at least partly explain the differences of the WL high peak counts seen in Zorrilla Matilla et al. (2016).

In this paper, we investigate in detail the LSS projection effect on WL high peak counts, and improve the model of F10 by taking the projection effect into the theoretical considerations. We perform extensive tests using numerical simulations, demonstrating the applicability of the improved model for future WL studies.

The rest of the paper is organized as follows. §2 presents the WL peak analyses, and the improved model for high peak abundances including the LSS projection effects. In §3, we show the simulation tests in detail and validate the model performance for different survey settings. Summary and discussions are given in §4.

2. MODELLING WEAK LENSING PEAK ABUNDANCE INCLUDING THE LSS PROJECTION EFFECT

2.1. Weak gravitational lensing effect

Photons are subjected to the gravity of cosmic structures, and deflected when they propagate toward us. As a result, the observed images differ from their original ones. This phenomenon is referred to as the gravitational lensing effect. In the WL regime, the effect leads to small changes of size and shape of the images.

Theoretically, the WL effect can be described by the lensing potential ϕ . Its gradient gives rise to the deflection angle, and the second derivatives are related directly to the observational consequence of the lensing effect. Specifically, the convergence κ and the shear γ , characterizing the size and the shape changes, respectively, are given by (Bartelmann & Schneider 2001)

$$\kappa = \frac{1}{2} \nabla^2 \phi, \quad (1)$$

$$\gamma_1 = \frac{1}{2} \left(\frac{\partial^2 \phi}{\partial x_1^2} - \frac{\partial^2 \phi}{\partial x_2^2} \right), \quad \gamma_2 = \frac{\partial^2 \phi}{\partial x_1 \partial x_2}, \quad (2)$$

where $\mathbf{x} = (x_1, x_2)$ is the two-dimensional angular vector. Under the Born approximation, the convergence κ is the projected density fluctuation weighted by the lensing kernel, and given by

$$\kappa(\mathbf{x}) = \frac{3H_0^2\Omega_m}{2} \int_0^{\chi_H} d\chi' \int_{\chi'}^{\chi_H} d\chi \left[p_s(\chi) \frac{f_K(\chi - \chi') f_K(\chi')}{f_K(\chi) a(\chi')} \right] \delta[f_K(\chi') \mathbf{x}, \chi'], \quad (3)$$

where χ is the comoving radial distance, $\chi_H = \chi(z = \infty)$, a is the cosmic scale factor, f_K is the comoving angular diameter distance, δ is the 3-D density fluctuation, and p_s is the source distribution function. The cosmological parameters H_0 is the Hubble constant.

Define the lensing window function as:

$$w(\chi') = \int_{\chi'}^{\chi_H} d\chi p_s(\chi) \frac{f_K(\chi - \chi')}{f_K(\chi)}, \quad (4)$$

the corresponding power spectrum of κ is then

$$C_\ell = \frac{9H_0^4\Omega_m^2}{4} \int_0^{\chi_H} d\chi' \frac{w^2(\chi')}{a^2(\chi')} P_\delta\left(\frac{\ell}{f_K(\chi')}, \chi'\right), \quad (5)$$

where P_δ is the power spectrum of 3-D matter density perturbations.

Observationally, the brightness quadrupole moment tensor of a source galaxy can be measured, and from that, the source ellipticity can be extracted. The WL effect on observed images can then be described by the Jacobian matrix of the lensing equation, which reads

$$\begin{aligned} \mathbf{A} &= \begin{pmatrix} 1 - \kappa - \gamma_1 & -\gamma_2 \\ -\gamma_2 & 1 - \kappa + \gamma_1 \end{pmatrix} \\ &= (1 - \kappa) \begin{pmatrix} 1 - g_1 & -g_2 \\ -g_2 & 1 + g_1 \end{pmatrix}, \end{aligned} \quad (6)$$

where $g_i = \gamma_i/(1 - \kappa)$ is the reduced shear. Considering the intrinsic ellipticity of a source galaxy, the observed ellipticity written in the complex form (Seitz & Schneider 1997) is

$$\epsilon = \begin{cases} \frac{\epsilon_s + \mathbf{g}}{1 + \mathbf{g}^* \epsilon_s}; & \text{for } |\mathbf{g}| \leq 1 \\ \frac{1 + \mathbf{g} \epsilon_s^*}{\epsilon_s^* + \mathbf{g}^*}, & \text{for } |\mathbf{g}| > 1 \end{cases} \quad (7)$$

where ϵ and ϵ_s are the observed and the intrinsic ellipticities of a source, respectively. The symbol $*$ represents the complex conjugate operation. It is seen that the observed ellipticity is closely related to the WL shear. For

$\kappa \ll 1$, $\epsilon \approx \epsilon_s + \gamma$. Without considering the intrinsic alignments, the correlation analyses of ϵ can thus give rise directly to an estimate of the WL shear correlation (e.g., Fu et al. 2008; Kilbinger et al. 2013; Fu et al. 2014; Jee et al. 2016; Becker et al. 2016; Hildebrandt et al. 2017).

Alternatively, because of the physical relation between the shear and the convergence as seen in Eq.(1) and Eq. (2), it is possible to reconstruct the convergence κ field from the observed ellipticities after a suitable smoothing (e.g., Kaiser 1993; Seitz & Schneider 1995; Bartelmann 1995; Squires & Kaiser 1996; Jullo et al. 2014). We note that κ is the weighted projection of the density fluctuations and thus the structures can be better seen visually in the κ field than that in the shear field. Comparing to previous observations targeting at individual clusters, the current survey cameras have a large field of view, typically $\sim 1^\circ \times 1^\circ$, and thus the boundary effects on the convergence reconstruction can be in good control. Cosmological studies using the reconstructed convergence fields have been carried out for different WL surveys (e.g., Shan et al. 2012; Van Waerbeke et al. 2013; Shan et al. 2014; J. Liu et al. 2015a; X. K. Liu et al. 2015b, 2016).

In this paper, we concentrate on WL peaks identified in convergence fields, and particularly study the LSS projection effects on high peak abundances.

2.2. WL high peak abundance with stochastic LSS

Physically, the WL convergence field reflects the projected density distribution weighted by the lensing kernel. Peaks there should correspond to the projected mass concentrations. Studies show that for a high peak, its signal is primarily contributed by a single massive halo located in the line of sight (e.g., Yang et al. 2011; X. K. Liu et al. 2014; Liu & Haiman 2016).

In Fig.1, we zoom in two high peaks from our ray-tracing simulations to be described in detail in §3. The horizontal axes are for the redshift of the lens planes, and the vertical axes show the relative contribution of each lens plane to the final peak signal $\mathcal{K}_{\text{peak}}$. The upper panels show the noiseless cases from ray-tracing simulations, and the lower panels are for the cases adding the shape noise from intrinsic ellipticities of source galaxies. The left ones are for a peak with the source galaxies at $z_s = 0.71$, and $n_g = 10 \text{ arcmin}^{-2}$. The insert in the lower panel shows the zoom-in local image of the noisy peak. Here we apply a Gaussian smoothing with the window function

$$W_{\theta_G}(\boldsymbol{\theta}) = \frac{1}{\pi\theta_G^2} \exp\left(-\frac{|\boldsymbol{\theta}|^2}{\theta_G^2}\right). \quad (8)$$

We take $\theta_G = 2.0 \text{ arcmin}$ in this paper. For this peak,

$\mathcal{K}_{\text{peak}} \approx 0.0835$ for the noiseless case (upper), and $\mathcal{K}_{\text{peak}} \approx 0.114$ for the noisy case (lower). It is seen clearly that the lens plane at $z \approx 0.18$ contributes dominantly to the peak signal. Further examination finds that there is a massive halo located there. In the noiseless case, the LSS effect from other lens planes only accounts for less than 10% (negative) of the peak signal as indicated by the black bar. In the noisy case, the dominant halo contributes $\sim 80\%$ of the peak signal. The shape noise as indicated by the blue bar contributes $\sim 25\%$, and LSS from other planes contributes $\sim -5\%$. The right panels are for the case with $z_s = 2.05$ and $n_g = 20 \text{ arcmin}^{-2}$. Here the dominant halo is at $z \approx 0.7$. In this case, the LSS effect increases to $\sim -15\%$ because of the increase of z_s . The shape noise contribution is $\sim 10\%$.

These two examples show that for high peaks, the halo approach to model the WL peak abundances is a physically viable approach. The shape noise and the LSS projection effect can be regarded as perturbations to the signal from the dominant halo. For relatively shallow surveys, the shape noise is much larger than the LSS effect, and we expect the good performance of the F10 model that takes into account the shape noise but without including the LSS effect. For deep surveys, however, the two perturbations are comparable, and the stochastic LSS effect cannot be neglected.

As a comparison, we show in Fig.2 a low peak with $z_s = 2.05$ and $n_g = 20 \text{ arcmin}^{-2}$. The peak signal is $\mathcal{K}_{\text{peak}} \approx 0.0422$. It is seen that the signals are from the cumulative effect of the line-of-sight mass distribution and no dominant halo contribution can be found. For these peaks, different modelling methodology other than the halo approach is needed.

In this paper, we focus on high peaks, and present our model for high peak abundances including LSS projection effects. Similar to F10, we assume that the signal of a true high peak is mainly from a single massive halo. The shape noise contributes a random component to the reconstructed convergence field. For stochastic LSS, from Fig.1, we see that they add onto the final peak signal in a zigzag way leading to a random perturbation statistically. Thus it is appropriate to model the LSS projection effect also as a random field. Therefore in our model, the convergence field in a halo region can be written as

$$\mathcal{K} = \mathcal{K}_H + \mathcal{K}_{\text{LSS}} + \mathcal{N}, \quad (9)$$

where \mathcal{K}_H is the contribution from the halo convolved with a window function corresponding to the smoothing operation made in the convergence reconstruction. It is regarded as a known quantity given the density profile of the halo. The smoothed shape noise field \mathcal{N} is

assumed to be Gaussian due to the central limit theorem (e.g., van Waerbeke 2000). We note that in general, the overall convergence field from simulations show non-Gaussianity due to the nonlinearity of structure formation. In our consideration here, however, \mathcal{K}_{LSS} is the stochastic LSS contribution excluding the massive halo part which is already explicitly split out as \mathcal{K}_H . It can be more Gaussian than the overall convergence field. Also \mathcal{K}_{LSS} is from small additive contributions from different lens planes in the high peak case and $|\mathcal{K}_{\text{LSS}}| \ll |\mathcal{K}_H|$. We therefore, as an approximation, assume that \mathcal{K}_{LSS} is also a Gaussian random field. Its validity will be extensively tested in §3 by comparing the model predictions for high peak counts with the results from simulations.

Similar consideration was mentioned in Shirasaki et al. (2015) but without really calculating the LSS contribution. Also, they only concentrate on the influence of the random field on the central peak signals of halos. In our modelling here, we take into account specifically the stochastic LSS, and calculate the total peak counts, including both the central ones from massive halos and the peaks from the random field $\mathcal{K}_{\text{LSS}} + \mathcal{N}$ inside halo regions as well as outside halo regions. In other words, to apply our model for cosmological studies, we can simply use all the high peaks identified from convergence maps without the need to go through additional analyses to locate true halo-associated peaks.

With the Gaussian assumptions for the two random fields, the total field \mathcal{K} in Eq.(9) is also a Gaussian random field. More specifically, it is the Gaussian random field $\mathcal{K}_{\text{LSS}} + \mathcal{N}$ modulated by the known halo contribution \mathcal{K}_H . Following the same procedures shown in F10, we can then calculate the number of peaks in a halo region. Two features need to be addressed. First, the original peak signal from the halo is affected by the existence of the two random fields, which not only generates scatters, but also leads to a positive shift for the signal (F10; Shirasaki et al. 2015). Secondly, the height distribution of peaks generated purely by the stochastic part $\mathcal{K}_{\text{LSS}} + \mathcal{N}$ is modulated by the halo convergence profile \mathcal{K}_H . With the halo mass function, we can then compute statistically the number of peaks per unit area in regions occupied by massive halos. For peaks outside the halo regions, we can calculate the peak abundances simply from the Gaussian field $\mathcal{K}_{\text{LSS}} + \mathcal{N}$.

In formulae, for high peak abundances, we have (F10)

$$n_{\text{peak}}(\nu) d\nu = n_{\text{peak}}^c(\nu) d\nu + n_{\text{peak}}^n(\nu) d\nu, \quad (10)$$

where $\nu = \mathcal{K}/\sigma_0$ with $\sigma_0^2 = \sigma_{\text{LSS},0}^2 + \sigma_{\text{N},0}^2$ being the total variance of the field $\mathcal{K}_{\text{LSS}} + \mathcal{N}$, $n_{\text{peak}}^c(\nu)$ and $n_{\text{peak}}^n(\nu)$ are, respectively, the number density of peaks per unit ν centered at ν in and outside halo regions.

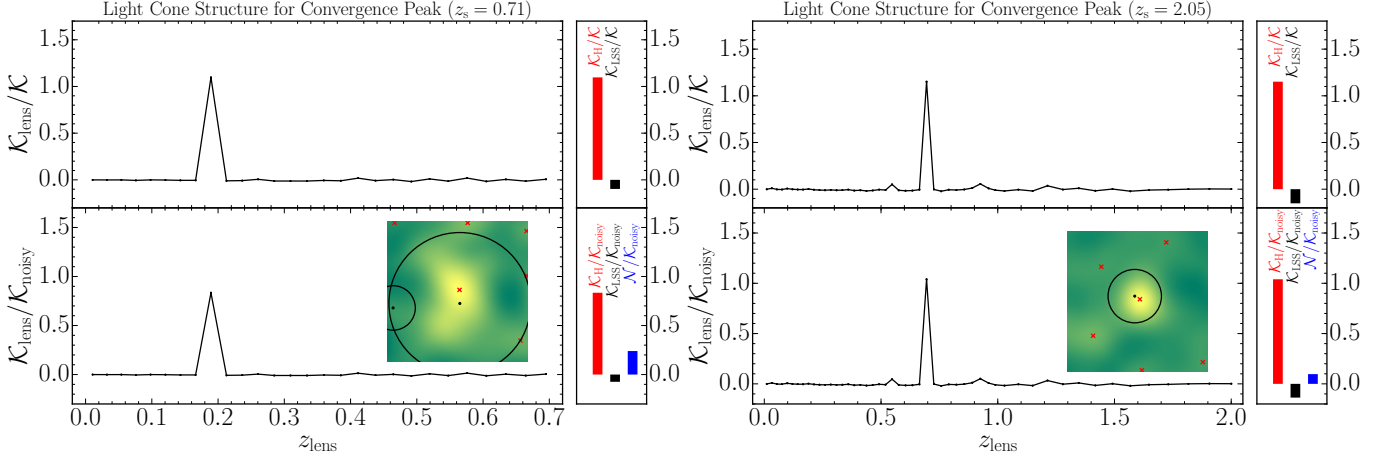


Figure 1. The light cone structures of two high peaks for $z_s = 0.71$ (left) and 2.05 (right), respectively. The two noisy peaks with signal-to-noise ratio $\nu_0 = 6.244$ (left) and $\nu_0 = 10$ (right). The upper panels show the contribution of each lens plane to the peak in noise free convergence map, i.e., the ratio $\mathcal{K}_{\text{lens}}/\mathcal{K}$ where $\mathcal{K} = \mathcal{K}_H + \mathcal{K}_{\text{LSS}}$. The contribution of the dominant halo is labelled as $\mathcal{K}_H/\mathcal{K}$ as red stick and the LSS projection is labelled as $\mathcal{K}_{\text{LSS}}/\mathcal{K}$ as black stick. The bottom panels are for the cases with shape noise added ($n_g = 10 \text{ arcmin}^{-2}$ for left and $n_g = 20 \text{ arcmin}^{-2}$ for right. The smoothing scales are both $\theta_G = 2.0 \text{ arcmin.}$) where $\mathcal{K}_{\text{noisy}} = \mathcal{K}_H + \mathcal{K}_{\text{LSS}} + \mathcal{N}$. The target peak is in the center of the corresponding stamp, labelled as red cross and the halos ($M \geq 10^{14.0} h^{-1} M_\odot$) are shown as the black circles with the sizes of their projected angular virial radii. The contribution of the shape noise $\mathcal{K}_N/\mathcal{K}_{\text{noisy}}$ is shown as the blue stick.

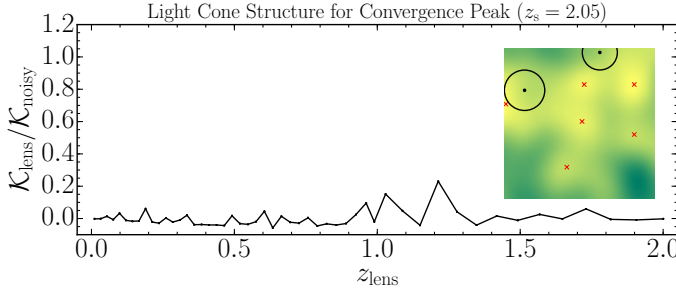


Figure 2. The light cone structure of a medium peak with the shape noise included ($z_s = 2.05$).

We emphasize that our model is applicable for high peaks in which the signals of true peaks are dominated by single massive halos (see Fig.1). Thus we consider halos with mass $M \geq M_*$ as major contributors to the halo regions. Simulation analyses show that $M_* \sim 10^{14} h^{-1} M_\odot$ is a proper choice. (Wei et al. 2018). The rest from smaller halos and the correlations between halos is included in the stochastic LSS part. Then for $n_{\text{peak}}^c(\nu)$, we have

$$n_{\text{peak}}^c(\nu) = \int dz \frac{dV(z)}{dz d\Omega} \int_{M_*}^\infty dM n(M, z) \times \int_0^{\theta_{\text{vir}}} d\theta (2\pi\theta) \hat{n}_{\text{peak}}^c(\nu, M, z, \theta), \quad (11)$$

where $n(M, z)$ is the comoving halo mass function, $\hat{n}_{\text{peak}}^c(\nu, M, z, \theta)$ is the number density of peaks at θ , and $\theta_{\text{vir}} = R_{\text{vir}}(M, z)/D_A(z)$ is the angular virial radius of a halo with mass M at redshift z . Here R_{vir} and D_A

are the virial radius of the halo and the angular diameter distance to the halo, respectively.

Considering the Gaussian random field $\mathcal{K}_{\text{LSS}} + \mathcal{N}$ modulated by the halo term \mathcal{K}_H , following the calculations in F10, we have

$$\begin{aligned} \hat{n}_{\text{peak}}^c(\nu, M, z, \theta) = & \exp \left[- \frac{(\mathcal{K}_H^1)^2 + (\mathcal{K}_H^2)^2}{\sigma_1^2} \right] \\ & \times \left[\frac{1}{2\pi\theta_*^2} \frac{1}{(2\pi)^{1/2}} \right] \exp \left[- \frac{1}{2} \left(\nu - \frac{\mathcal{K}_H}{\sigma_0} \right)^2 \right] \\ & \times \int_0^\infty dx \left\{ \frac{1}{[2\pi(1-\gamma^2)]^{1/2}} \right. \\ & \times \exp \left[- \frac{[x + (\mathcal{K}_H^{11} + \mathcal{K}_H^{22})/\sigma_2 - \gamma(\nu - \mathcal{K}_H/\sigma_0)]^2}{2(1-\gamma^2)} \right] \\ & \left. \times F(x) \right\} \end{aligned} \quad (12)$$

and

$$\begin{aligned} F(x) = & \exp \left[- \frac{(\mathcal{K}_H^{11} - \mathcal{K}_H^{22})^2}{\sigma_2^2} \right] \times \\ & \int_0^{1/2} de 8(x^2 e) x^2 (1 - 4e^2) \exp(-4x^2 e^2) \times \\ & \int_0^\pi \frac{d\psi}{\pi} \exp \left[- 4xe \cos(2\psi) \frac{(\mathcal{K}_H^{11} - \mathcal{K}_H^{22})}{\sigma_2} \right]. \end{aligned} \quad (13)$$

Here $\theta_*^2 = 2\sigma_1^2/\sigma_2^2$, $\gamma = \sigma_1^2/(\sigma_0\sigma_2)$, $\mathcal{K}_H^i = \partial_i \mathcal{K}_H$, and $\mathcal{K}_H^{ij} = \partial_{ij} \mathcal{K}_H$. Different from that in F10, here the quantities σ_i^2 ($i = 0, 1, 2$) are, respectively, the moments of the total random field $\mathcal{K}_{\text{LSS}} + \mathcal{N}$ and its first and second

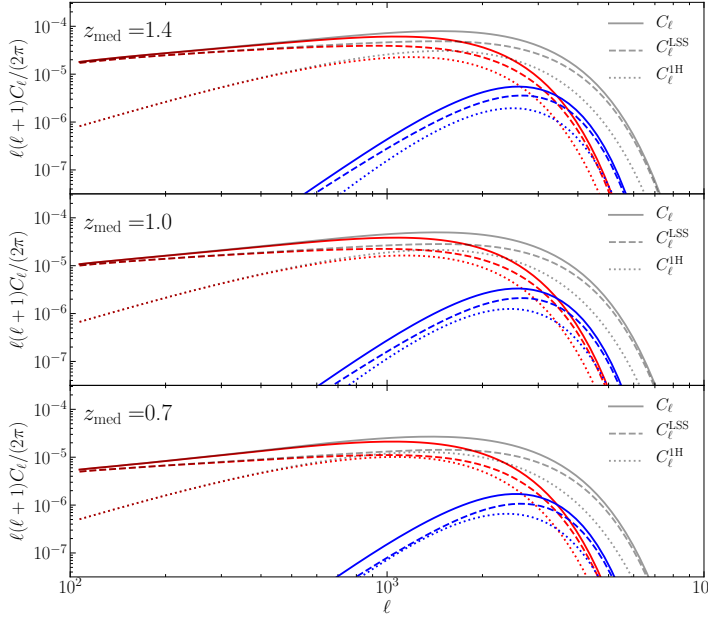


Figure 3. Weak lensing power spectra (gray), and the ones under Gaussian smoothing (red) and the U filtering (blue). The dashed and the dotted lines are the contributions of the LSS and the one-halo term from halos with $M \geq M_*$. The smoothing scale $\theta_G = \theta_U = 2.0$ arcmin is applied. The redshifts are $z_{\text{med}} = 1.4, 1.0$ and 0.7 , respectively, from top to bottom. The cosmological parameters are $(\Omega_m, \Omega_\Lambda, \Omega_b, h, n_s, \sigma_8) = (0.28, 0.72, 0.046, 0.7, 0.96, 0.82)$

derivatives. Specifically, $\sigma_i^2 = \sigma_{\text{LSS},i}^2 + \sigma_{\text{N},i}^2$.

For the number density of peaks contributed by those outside halo regions, $n_{\text{peak}}^n(\nu)$, we have

$$n_{\text{peak}}^n(\nu) = \frac{1}{d\Omega} \times \left\{ n_{\text{ran}}(\nu) \left[d\Omega - \int dz \frac{dV(z)}{dz} \int_{M_*}^\infty dM n(M, z) (\pi \theta_{\text{vir}}^2) \right] \right\}, \quad (14)$$

where $n_{\text{ran}}(\nu)$ is the number density of peaks from the random field $\mathcal{K}_{\text{LSS}} + \mathcal{N}$ without halo modulations, and it can be calculated from Eq.(12) by setting the halo related quantities to be zero.

From the above, we see that the stochastic LSS effects occur specifically in quantities of $\sigma_i^2 = \sigma_{\text{LSS},i}^2 + \sigma_{\text{N},i}^2$. For the shape noise part, we have (e.g. van Waerbeke 2000)

$$\sigma_{\text{N},i}^2 = \int_0^\infty \frac{\ell d\ell}{2\pi} \ell^{2i} C_\ell^{\text{N}}, \quad (15)$$

where C_ℓ^{N} is power spectrum of the smoothed noise field \mathcal{N} . For the Gaussian smoothing, we have

$$\sigma_{\text{N},0}^2 = \frac{\sigma_\epsilon^2}{4\pi n_g \theta_G^2}, \quad (16)$$

where σ_ϵ is the rms amplitude of the intrinsic ellipticities. We further have $\sigma_{\text{N},0} : \sigma_{\text{N},1} : \sigma_{\text{N},2} = 1 : \sqrt{2}/\theta_G :$

$2\sqrt{2}/\theta_G^2$.

For $\sigma_{\text{LSS},i}$, they are physical quantities and need to be computed in a cosmology-dependent way. In other words, $\sigma_{\text{LSS},i}$ also contributes to the cosmological information embedded in WL peak counts. Given a power spectrum for LSS convergence field, C_ℓ^{LSS} , we have

$$\sigma_{\text{LSS},i}^2 = \int_0^\infty \frac{\ell d\ell}{2\pi} \ell^{2i} C_\ell^{\text{LSS}}. \quad (17)$$

To calculate C_ℓ^{LSS} , we adopt the following approach. From Eq.(5), the WL power spectrum C_ℓ can be obtained from the integration of the weighted 3-D nonlinear power spectrum P_δ . For P_δ , it can be computed using the simulation-calibrated halo model (Takahashi et al. 2012) and has been included in different numerical packages, such as CAMB (Lewis et al. 2000). In the language of halo model, the overall P_δ consists of contributions from one-halo term of all halos and the two-halo term considering the correlations between halos. In our model here, halos with $M \geq M_*$ have been separated out as \mathcal{K}_H . Thus to compute the left-over stochastic LSS effects, we subtract the one-halo term from halos with $M \geq M_*$ from the overall power spectrum:

$$P_\delta^{\text{LSS}}[k, \chi(z)] = P_\delta[k, \chi(z)] - P_\delta^{\text{1H}} \Big|_{M \geq M_*} [k, \chi(z)]. \quad (18)$$

It is seen that P_δ^{LSS} contains the one-halo term from halos with $M < M_*$ and the two-halo term between all the halos including the ones with $M \geq M_*$. For the one-halo term $P_\delta^{\text{1H}} \Big|_{M \geq M_*}$, we have (e.g. Cooray & Sheth 2002)

$$P_\delta^{\text{1H}} \Big|_{M \geq M_*} [k, \chi(z)] = \frac{4\pi}{\bar{\rho}^2} \int_{M_*}^\infty dM M^2 W^2(k, M) n(M, z), \quad (19)$$

where $\bar{\rho}$ is the mean matter density of the universe, $W(k, M)$ is the Hankel transformation of the spherically symmetric halo density profile $\rho(r, M)$, given by

$$W(k, M) = \frac{1}{M} \int_0^{R_{\text{vir}}} dr \frac{\sin(kr)}{kr} 4\pi r^2 \rho(r, M). \quad (20)$$

From P_δ^{LSS} , we can obtain C_ℓ^{LSS} by

$$C_\ell^{\text{LSS}} = \frac{9H_0^4 \Omega_m^2}{4} \int_0^{\chi_H} d\chi' \frac{w^2(\chi')}{a^2(\chi')} P_\delta^{\text{LSS}}\left(\frac{\ell}{f_K(\chi')}, \chi'\right), \quad (21)$$

and subsequently $\sigma_{\text{LSS},i}^2$ by Eq.(17).

For the calculations of one-halo term in Eq.(19), we take the Navarro-Frenk-White (NFW) halo density profile given by (Navarro et al. 1996, 1997)

$$\rho(r) = \frac{\rho_s}{(r/r_s)(1+r/r_s)^2}, \quad (22)$$

where ρ_s and r_s are the characteristic density and scale

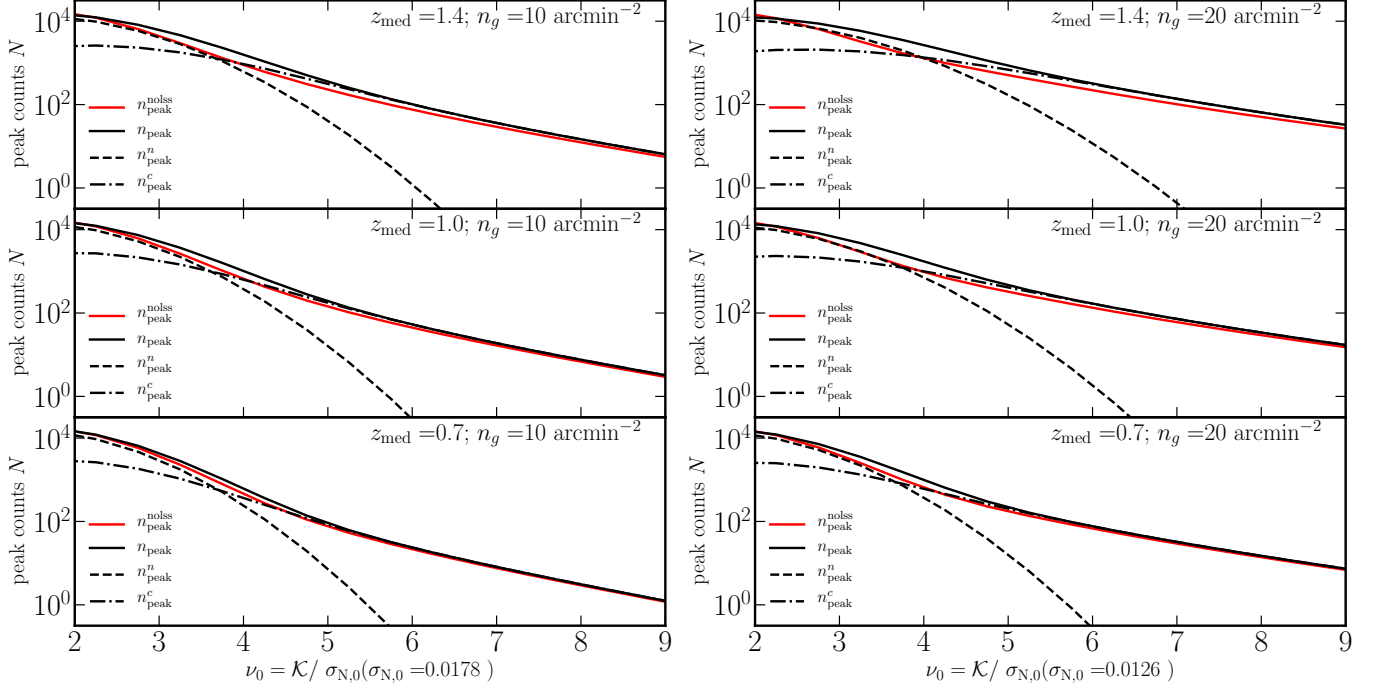


Figure 4. Model predictions from F10 (red lines) and from our model considering LSS projection effect (black lines) with different z_{med} . From top to bottom $z_{\text{med}} = 1.4, 1.0$ and 0.7 , respectively and the sky area is $\approx 1080 \text{ deg}^2$. The cosmological parameters are $(\Omega_m, \Omega_\Lambda, \Omega_b, h, n_s, \sigma_8) = (0.28, 0.72, 0.046, 0.7, 0.96, 0.82)$. The components n_{peak}^n and n_{peak}^c of total n_{peak} with LSS projection effect included are shown in dashed lines and dashed-dotted lines, respectively. The smoothing scale is $\theta_G = 2.0$ arcmin, the source number density $n_g = 10 \text{ arcmin}^{-2}$ (left panel) and 20 arcmin^{-2} (right panel)

of a halo, respectively. The scale r_s reflects the compactness of a halo, and is often given through the concentration parameter $c_{\text{th}} = R_{\text{th}}/r_s$ with R_{th} being the radius inside which the average density of a halo is Δ_{th} times the cosmic density. Here we adopt the virial radius R_{vir} , and use the concentration-mass relation from Duffy et al. (2008) with

$$c_{\text{vir}}(M, z) = 5.72 \left(\frac{M}{10^{14} h^{-1} M_\odot} \right)^{-0.081} (1+z)^{-0.71}. \quad (23)$$

For the halo mass function $n(M, z)$, we use the one given in Watson et al. (2013), an empirical fitting formula derived from N -body simulations.

In Fig.3, we show C_ℓ^{LSS} together with the overall C_ℓ and the massive one-halo term C_ℓ^{1H} under different source galaxy distributions $p(z)$, for which we adopt the following form

$$p(z) \propto z^2 \exp \left[- \left(1.414 \frac{z}{z_{\text{med}}} \right)^{1.5} \right], \quad (24)$$

where z_{med} is the median redshift. In the plots, we also show the power spectra of aperture mass under the U filtering (blue) to be discussed in Sec.3.4. Here we focus on the Gaussian filter case (red). We see that on large scales, C_ℓ^{LSS} is very close to C_ℓ . On small scales with $\ell \sim 2000$, the LSS random field C_ℓ^{LSS} is small than the

overall convergence field C_ℓ due to the exclusion of the one-halo term from halos with $M \geq 10^{14.0} h^{-1} M_\odot$

With Eq.(10) to Eq.(21), the number density of high peaks taking into account the LSS projection effects can be computed. In Fig.4, we show the results from this model (solid lines) and the ones from F10 without the LSS (red lines). For the model with LSS effects, we also show the contributions of peaks in (n_{peak}^c , dashed-dotted) and outside (n_{peak}^n , dashed) halo regions. It is seen that in the considered cases, peaks with $\nu_0 \gtrsim 4$ are dominantly from halo regions. For higher z_{med} , such domination shifts a little more toward higher ν_0 .

We note that in our model calculation, we directly obtain peak counts at different $\nu = K/\sigma_0$. On the other hand, observationally, we can only estimate the shape noise part $\sigma_{N,0}$ by randomly rotating the observed galaxies. Thus to be consistent with observational analyses, we first make a binning in terms of $\nu_0 = K/\sigma_{N,0}$ and then convert it to the binning in ν using the ratio of $\sigma_{N,0}/\sigma_0$ for model calculations. The shown results are the peak counts versus ν_0 . The corresponding K are also listed in the upper horizontal axis. It is seen clearly that with the increase of the median redshift of source galaxies, the LSS projection effects become increasingly important.

In the next section, we will compare our theoretical re-

sults with those from ray-tracing simulations to validate the model performance.

3. SIMULATION TESTS

In this section, we test our model performance using ray-tracing simulations. We describe the simulations and the mock WL data generation with respect to different source galaxy distributions in §3.1, and present the comparison results in detail in §3.2.

3.1. WL Simulations

We carry out ray-tracing simulations up to $z = 3.0$ based on large sets of N -body simulations. The simulation setting is the same as that in X. K. Liu et al. (2015b), but with the number of simulations doubled. The fiducial cosmology is the flat Λ CDM model with the parameters of Ω_m , dark energy density Ω_Λ , baryonic matter density Ω_b , Hubble constant h , the power index of initial matter density perturbation power spectrum n_s , and σ_8 set to be $(\Omega_m, \Omega_\Lambda, \Omega_b, h, n_s, \sigma_8) = (0.28, 0.72, 0.046, 0.7, 0.96, 0.82)$.

For each set of ray-tracing calculations, we use 12 independent N -body simulation boxes to fill up to the region of a comoving distance $\sim 4.5 h^{-1} \text{Gpc}$ to $z = 3.0$, as illustrated in Fig.5. Among them, eight small boxes each with the size of $320 h^{-1} \text{Mpc}$ are padded between $z = 0.0$ and $z = 1.0$. In the reshift range of $1.0 < z \leq 3.0$, we pad four boxes of size $600 h^{-1} \text{Mpc}$. The number of particles of N -body simulations for both small and large boxes is 640^3 , and the corresponding mass resolution is $\sim 9.7 \times 10^9 h^{-1} M_\odot$ and $\sim 6.4 \times 10^{10} h^{-1} M_\odot$, respectively. For each of the boxes, we start at $z = 50$ and generate the initial conditions using 2LPTic¹ based on the initial power spectrum from CAMB² (Lewis et al. 2000). The simulations are run by GADGET-2³ (Springel 2005) with the force softening length being $\sim 20 h^{-1} \text{kpc}$.

In the multi-plane ray-tracing calculations, up to $z = 3$, we use 59 lens planes with the corresponding redshifts z_l being listed in Table 1. We run the ray-tracing WL simulations using the same code described in X. K. Liu et al. (2014) in which we deal with the crossing-boundary problem of halos following the procedures used in Hilbert et al. (2009). We then generate $4 \times (3.5^\circ \times 3.5^\circ)$ convergence and shear maps at each lens plane, denoted as $\kappa(z_{\text{lens}})$ and $\gamma_i(z_{\text{lens}})$, respectively, from a set of 12 N -body simulations. Each of the $3.5^\circ \times 3.5^\circ$ maps is pixelized into 1024×1024

Table 1. Redshifts of the lens planes.

0.0107	0.0322	0.0540	0.0759	0.0981	0.1205
0.1432	0.1661	0.1893	0.2127	0.2364	0.2604
0.2847	0.3094	0.3343	0.3596	0.3853	0.4113
0.4377	0.4645	0.4917	0.5193	0.5474	0.5759
0.6049	0.6344	0.6645	0.6950	0.7261	0.7578
0.7900	0.8229	0.8564	0.8906	0.9254	0.9610
0.9895	1.0289	1.0882	1.1496	1.2131	1.2789
1.3472	1.4180	1.4915	1.5680	1.6475	1.7303
1.8166	1.9066	2.0005	2.0987	2.2013	2.3087
2.4213	2.5393	2.6632	2.7934	2.9296	

grids with the pixel size of $\sim 0.205 \text{ arcmin}$. We perform in total 24 sets of N -body simulations, which give rise to $24 \times 4 \times (3.5^\circ \times 3.5^\circ) = 1176 \text{ deg}^2$ of $\kappa(z_{\text{lens}})$ and $\gamma_i(z_{\text{lens}})$. From them, we construct the final κ (or γ) maps corresponding to different source galaxy distributions as follows

$$\kappa_{\text{mock}}(\boldsymbol{\theta}) = \sum_{\text{lens}} p(z_{\text{lens}}) \kappa(\boldsymbol{\theta}; z_{\text{lens}}) (z_{\text{lens}+1} - z_{\text{lens}}), \quad (25)$$

where $p(z)$ is the normalized source galaxy redshift distribution given in Eq.(24). For a given $p(z)$, we obtain $24 \times 4 = 96$ maps, each with the size of $3.5^\circ \times 3.5^\circ$.

Because we aim at testing our WL high peak model, we concentrate on convergence maps directly here. We include the shape noise by adding a Gaussian noise field to the pixels of each of $24 \times 4 = 96$ convergence maps $\kappa_{\text{mock}}(\boldsymbol{\theta})$ with the variance given by

$$\sigma_{\text{pix}}^2 = \frac{\sigma_\epsilon^2}{2n_g \theta_{\text{pix}}^2}, \quad (26)$$

where we take $\sigma_\epsilon = 0.4$ and the pixel size of maps $\theta_{\text{pix}} = 0.205 \text{ arcmin}$. We then apply a Gaussian smoothing given by Eq.(8) with $\theta_G = 2.0 \text{ arcmin}$ to obtain the final smoothed noisy convergence maps for peak analyses.

3.2. Model test

To analyze the LSS effects and test our model performance, we consider different survey parameters, including the median redshift z_{med} , the number density n_g of the source galaxies and the survey area S . These are listed in Table 2.

From our simulations, for each set of (z_{med}, n_g) , we generate 96 noiseless convergence maps each with the size of $3.5^\circ \times 3.5^\circ$. For each map, we then add a Gaussian shape noise field and apply smoothing as described above. To suppress the fluctuations caused by a particular realization of the noise field, we perform noise adding

¹ <http://cosmo.nyu.edu/roman/2LPT/>

² <http://camb.info/>

³ <http://wwwmpa.mpa-garching.mpg.de/gadget/>

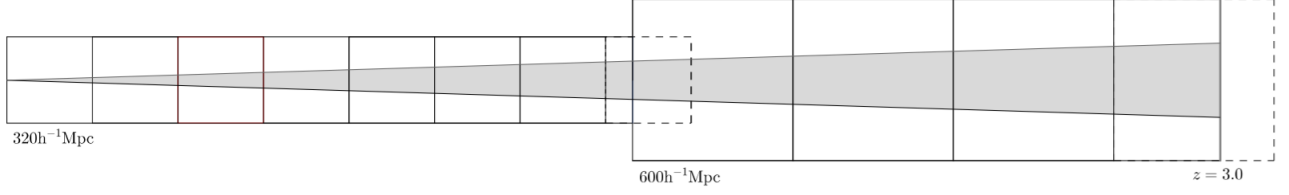


Figure 5. An illustration of the ray-tracing design from $z = 0$ to $z = 3$.

Table 2. Survey parameters for mocks.

z_{med}	$n_g(\text{arcmin}^{-2})$	$\theta_G(\text{arcmin})$	$S(\text{deg}^2)$	Mock Name
	10	2.0	150	S10small
0.7	10	2.0	≈ 1086	S10
	20	2.0	≈ 1086	S20
1.0	20	2.0	≈ 1086	M20
1.4	20	2.0	≈ 1086	D20

20 times for each map with different seeds. Therefore in total, we have 20×96 maps with the shape noise included for each set of (z_{med}, n_g) .

We first compare peak counts between model predictions and the simulation results. We identify a peak in a pixelized convergence map from simulations if its convergence value is higher than those of its eight neighboring pixels. Because Fourier transformations are involved in ray-tracing calculations and in the smoothing operations, there can be boundary effects in each of the $3.5^\circ \times 3.5^\circ$ convergence maps. To avoid such a problem, in our peak analyses, we exclude the outermost 20 pixels along each side of the map. The left-over area is $\sim 11.31 \text{ deg}^2$ for each map, and the total is $\sim 96 \times 11.31 \approx 1086 \text{ deg}^2$ for each set of noise field realizations.

For our theoretical model calculations, the quantity M_* corresponds to the lower mass limit of halos above which the halos dominate the WL high peak signals. We have performed χ^2 tests with respect to the simulated peak counts to find suitable M_* . We note that for $z_{\text{med}} = 0.7$ and $n_g = 10 \text{ arcmin}^{-2}$, the shape noise is much larger than that of the LSS effects, and the model of F10 works equally well. In that case using F10, $M_* = 10^{13.9} h^{-1} M_\odot$ gives results that are in good agreement with those from simulations. In our current model with the LSS effects, for all the cases including the one with $z_{\text{med}} = 0.7$ and $n_g = 10 \text{ arcmin}^{-2}$, $M_* = 10^{14.0} h^{-1} M_\odot$ is a proper choice. We comment that physically, the suitable choice of M_* depends on the halo mass function used in the model calculations. The specific value of M_* may also have a mild cosmology-dependence, which may need to be taken into account in future for very high precision studies. In this paper, we do not include this subtle effect.

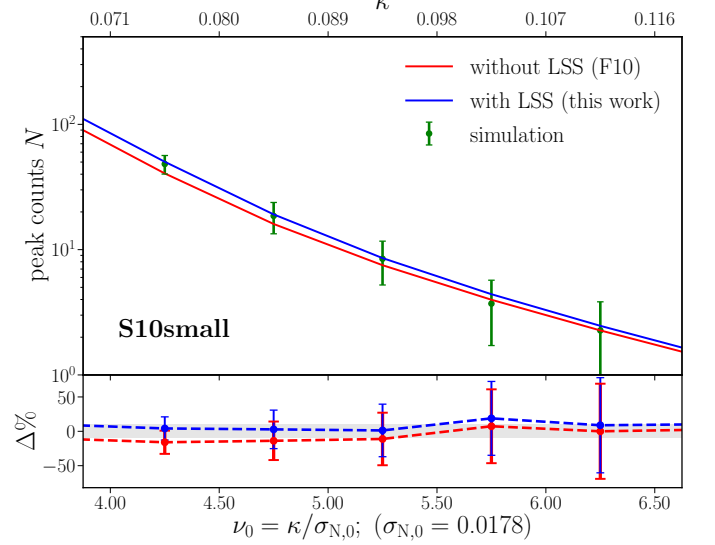


Figure 6. Model prediction and the peak counts from simulation for **S10small**. The red line is model prediction from F10 and the blue line is the prediction from our model. Green dots with error bars are peak counts from simulation. The relative differences between simulation results and model predictions are shown in the bottom panel.

The peak count comparison results are shown in Fig.6 and Fig.7 corresponding to the survey conditions listed in Table 2 respectively. The green symbols are the results averaged over the corresponding 20×96 maps and then scaled to the considered survey area. The error bars are the corresponding Poisson errors. The blue lines are the results from our model including the LSS effect, and the red lines are from F10 without the LSS effect. Again, the shown results are the peak counts vs. ν_0 defined by the shape noise $\sigma_{N,0}$. The corresponding κ are indicated in the upper horizontal axes. In the bottom part of each panel, we show the fractional differences of the two models with respect to the simulation results.

Fig.6 shows the results for **S10small** with $z_{\text{med}} = 0.7$, $n_g = 10 \text{ arcmin}^{-2}$, and $S = 150 \text{ deg}^2$, similar to the current accomplished WL surveys. In this case, $\sigma_{\text{LSS},0} = 0.0057$ and $\sigma_{N,0} = 0.0178$ for $\theta_G = 2.0 \text{ arcmin}$. Thus the contribution from LSS is much smaller than that from the shape noise, and its effect on WL peak counts is rather weak considering relatively large error bars. This can be evidently seen from the lower part of the panel.

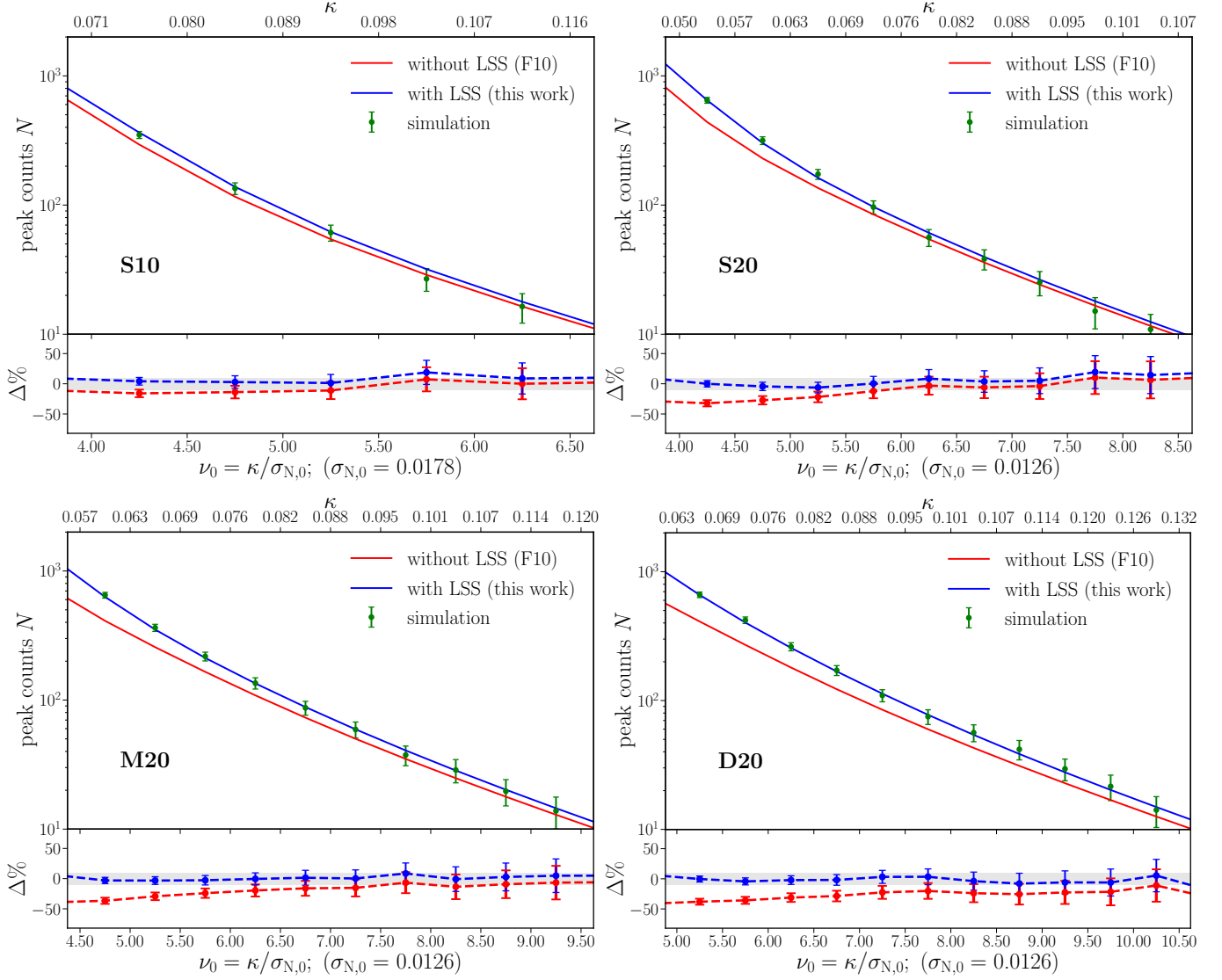


Figure 7. The same as in Fig.6 but for the cases of **S10** (upper left), **S20** (upper right), **M20** (bottom left) and **D20** (bottom right).

Both the blue and red lines agree with the simulation results very well for high peaks with $\nu_0 \geq 4$ with the fractional differences less than 10%.

In the upper left panel of Fig.7, we show the results of **S10**. In this case, the number density and the redshift distribution of source galaxies are the same as those in Fig.6, but with a larger survey area with $S = 1086 \text{ deg}^2$. Thus the statistical errors of WL peak counts are smaller by ~ 2.7 times than that of **S10small**. We see again that both models work well, and the model including the LSS effect (blue) gives better results for the left two bins.

In the upper right panel of Fig.7, the results of **S20** with $z_{\text{med}} = 0.7$, $n_g = 20 \text{ arcmin}^{-2}$, and $S = 1086 \text{ deg}^2$ are presented. In this case, the LSS effect is the same as that of **S10**, but the shape noise is lower with

$\sigma_{N,0} = 0.0126$. Thus the relative contribution of the LSS effect should be stronger than the case of **S10**. We see that for $\nu_0 > 5$, although both the blue line and the red line agree with the simulation results within 10%, the red line is systematically lower, showing that the LSS effect starts to be important. For $\nu_0 < 5$, the red line deviates significantly from the simulation results, but our current model including the LSS effect can give excellent predictions out to $\nu_0 \sim 4$.

The results for **M20** with $z_{\text{med}} = 1.0$, $n_g = 20 \text{ arcmin}^{-2}$ and $S = 1086 \text{ deg}^2$ are shown in the lower left panel of Fig.7. Here the LSS contribution increases to $\sigma_{\text{LSS},0} = 0.0082$. Comparing to the upper right panel, we see that the model prediction without the LSS effect (red line) significantly underestimates the peak counts over the whole considered range. Taking into account

the LSS effect, our improved model works very well to $\mathcal{K} \gtrsim 0.06$, corresponding to $\nu_0 \gtrsim 4.5$.

With even higher z_{med} , the LSS projection effect gets larger. The lower right panel of Fig.7 shows the results of **D20** with $z_{\text{med}} = 1.4$, $n_g = 20 \text{ arcmin}^{-2}$ and $S = 1086 \text{ deg}^2$. In this case, $\sigma_{\text{LSS},0} = 0.0108$, is comparable to that from the shape noise with $\sigma_{\text{N},0} = 0.0126$. Without including the LSS projection effect, the underestimate is at the level of 30%, much larger than the statistical errors. While including the LSS effect, the model predictions (blue lines) are in excellent agreement with the simulation results to $\mathcal{K} \gtrsim 0.063$, or $\nu_0 \gtrsim 5$.

Note that for the three cases with $n_g = 20 \text{ arcmin}^{-2}$, the WL lensing signal from a halo increases with the increase of z_{med} . Thus we see a somewhat increase of the lower limit of ν_0 above which our high-peak halo model applies from $z_{\text{med}} = 0.7$ to $z_{\text{med}} = 1.4$.

3.3. Cosmological constraints

To demonstrate explicitly the LSS effect on the cosmological constraints derived from WL high peak counts and how our improved model performs, here we run MCMC fitting using WL mock data.

For **S10**, **S20**, **M20** and **D20** in Table 2, we generate, respectively, the WL peak count mock data by averaging over the 20×96 maps. For **S10small**, we scale the peak counts obtained for **S10** to $S = 150 \text{ deg}^2$. The central data points in different bins $\{N_i\}$ for different cases are the same as those shown in Fig.6 and in Fig.7. Note that for the upper end of the peaks, we only use bins with $N_i \gtrsim 10$.

We employ the χ^2 fitting to constrain cosmological parameters from WL mock data. The χ^2 is defined as

$$\chi^2 = \Delta^T \widehat{\mathbf{C}}^{-1} \Delta, \quad (27)$$

where Δ is $\Delta \equiv \mathbf{N} - \widehat{\mathbf{N}}$ with \mathbf{N} being the mock data vector consisting of WL peak counts of different bins and $\widehat{\mathbf{N}}$ being the model predictions for these bins. The quantity \mathbf{C} is the covariance matrix for peak counts between different bins. We calculate it using the simulation at the fiducial cosmology. Specifically, for each case in Table 2, we first obtain the covariance for an area S_0 corresponding to an individual simulated convergence map by calculating the variance of peaks $[\mathbf{C}_0]_{ij}$ between i th bin and j th bin from 20×96 maps. We then scale \mathbf{C}_0 to the mock survey area S considered in different cases by

$$\mathbf{C} = \frac{S}{S_0} \mathbf{C}_0. \quad (28)$$

Studies have shown that this scaling can lead to a

slight underestimate of the covariance for large S (Kraichvil et al. 2010). This, however, should not affect our conclusions regarding the bias resulting from neglecting the LSS effect and the validity of our new model. It is also noted that the cosmology-dependence of the covariance is not considered here.

From \mathbf{C} , we can calculate its inverse \mathbf{C}^{-1} and further the $\widehat{\mathbf{C}}^{-1}$:

$$\widehat{\mathbf{C}}^{-1} = \frac{R - N_{\text{bin}} - 2}{R - 1} \mathbf{C}^{-1}, \quad (29)$$

where $R = 20 \times 96$ and N_{bin} is the number of bins of WL peak counts used in deriving cosmological constraints.

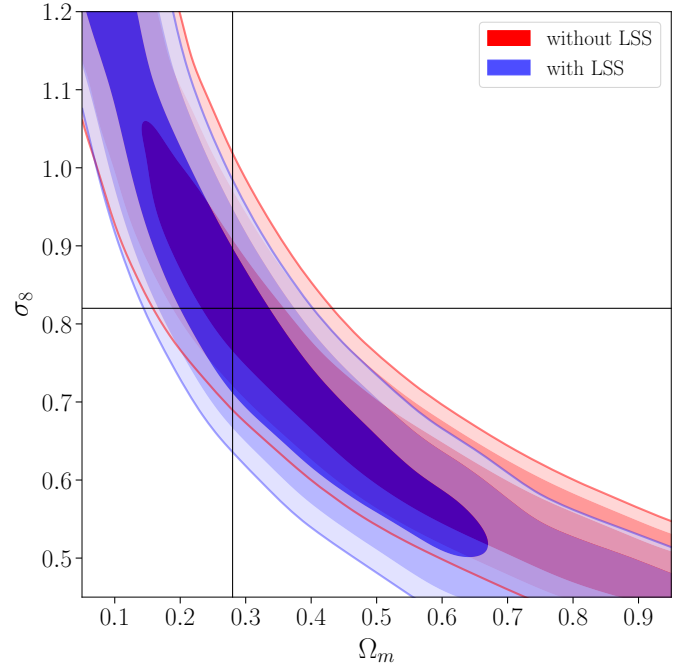


Figure 8. The derived cosmological constraints for **S10small**. The red contours are the constraining results of $1 - \sigma$, $2 - \sigma$ and $3 - \sigma$ using **F10** model and the blue ones are from the model in this work. The input cosmological parameters for simulation is indicated by green crossing lines.

In our analyses here, we concentrate on the constraints on Ω_m and σ_8 , and set all the other cosmological parameters fixed to be the input values of the simulations. We implement the MCMC technique to explore the posterior probabilities of (Ω_m, σ_8) (X. K. Liu et al. 2015b, 2016).

The constraining results for **S10small** are shown in Fig.8, where the blue and red contours are the results using the model presented in this paper including the LSS effect and the model of **F10** without the LSS effect, respectively. The green cross indicates the input values of the two parameters for WL simulations. Consistent with that shown in Fig.6, the two constraints overlap significantly and the two models perform equally well.

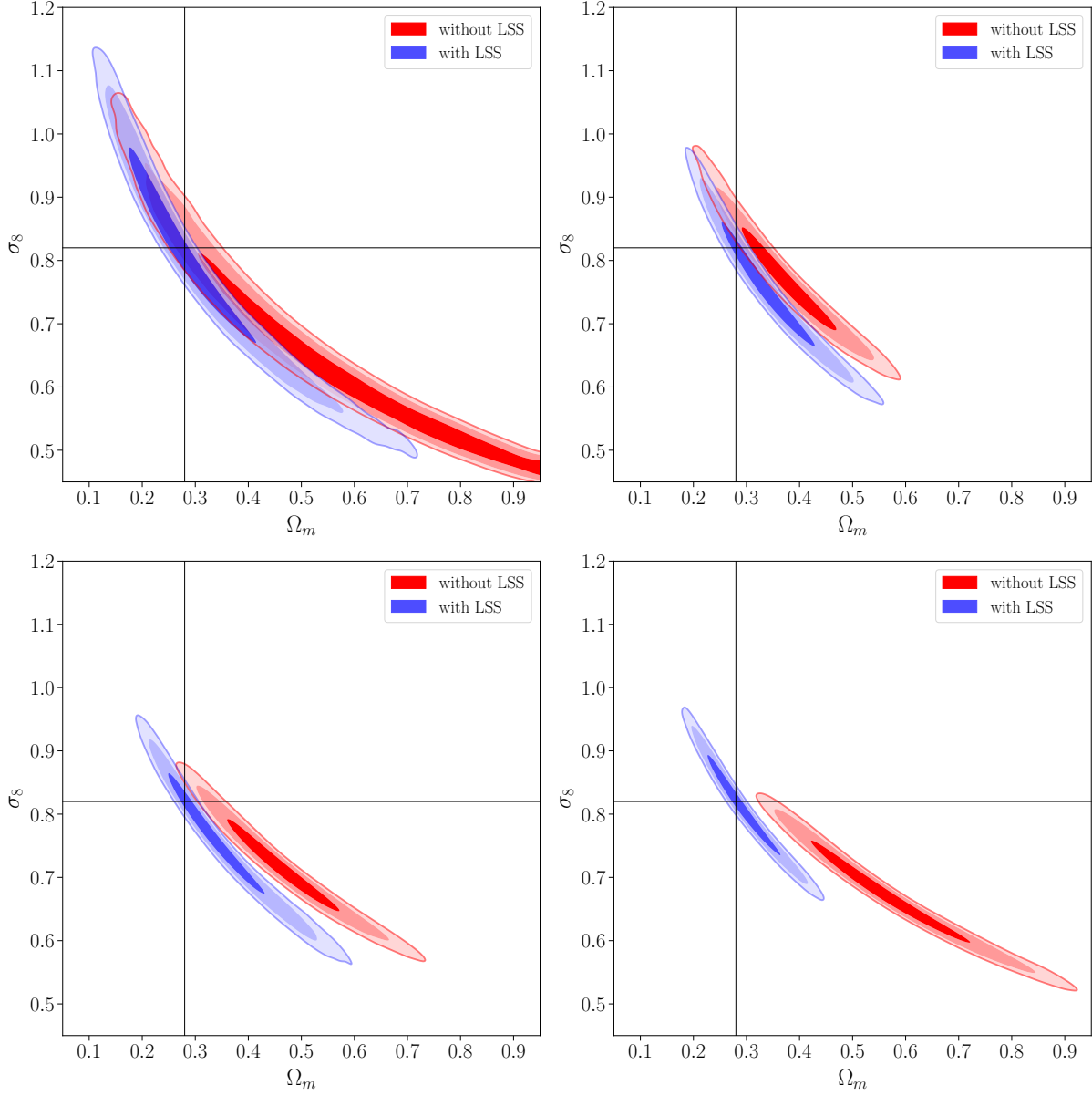


Figure 9. Results for mock **S10** (upper left), **S20** (upper right), **M20** (lower left) and **D20** (lower right), respectively.

Table 3. Degeneracy parameter (α, Σ_8) for different cases. The degeneracy is defined by $\Sigma_8 = \sigma_8(\Omega_m/0.27)^\alpha$.

Mocks	S10small ^a	S10small	S10	S20	M20	D20
α	0.434	0.452	0.456	0.493	0.465	0.417
Σ_8	0.833 ± 0.045	0.791 ± 0.050	0.814 ± 0.016	0.836 ± 0.011	0.838 ± 0.009	0.834 ± 0.008

^a derived from **F10** model.

In this case, the LSS effect is negligible, and the application of **F10** model is well justified without introducing notable biases in the parameter constraints.

The results for **S10**, **S20**, **M20** and **D20** are presented in Fig.9. Because of the survey area being larger than that of **S10small**, the statistical errors are reduced considerably resulting smaller contours. For **S10** (upper

left), the blue and red contours still have a large overlap. The WL simulation input values are at the edge of the $1 - \sigma$ red region. The blue constraints from our improved model including the LSS effect, on the other hand, give better results.

For **S20** (upper right), $\sigma_{N,0} = 0.0126$, $\sigma_{LSS,0} = 0.0057$, and the total $\sigma_0 = 0.0138$. The fractional con-

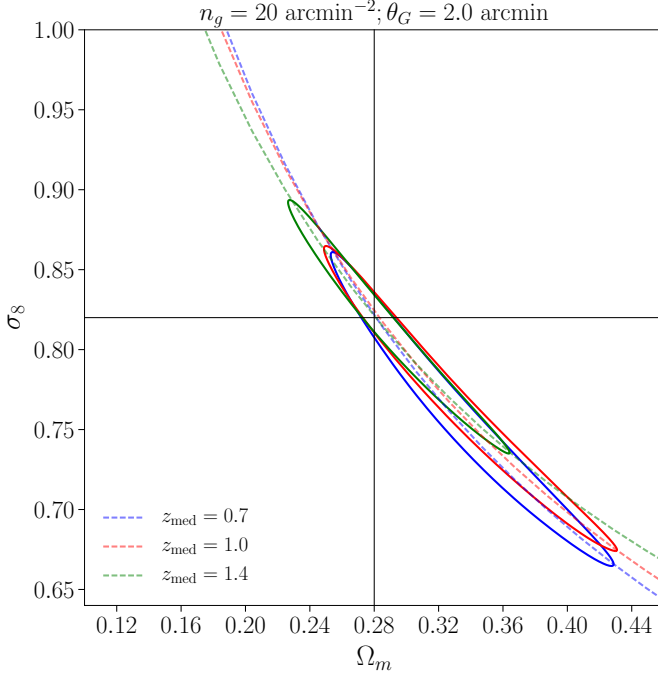


Figure 10. The degeneracy of (Ω_m, σ_8) . The contours are the 1σ regions from the peak abundance model including LSS projection for **S20**, **M20** and **D20**. The dashed lines are the corresponding fitted degeneracy curves defined by $\Sigma_8 = \sigma_8(\Omega_m/0.27)^\alpha$. The input cosmological parameters for mock data are shown as the black cross.

tribution from LSS is $\sigma_{\text{LSS},0}/\sigma_0 \approx 0.41$. Thus the LSS effect is already apparent. The constraints obtained by using the model of [F10](#) are biased by more than 2σ . For **M20** (lower left) and **D20** (lower right), the shape noise is the same as that of **S20**. But the LSS effect is stronger with $\sigma_{\text{LSS},0} = 0.0082$ and 0.0109 , and the corresponding fractional contribution to σ_0 is ~ 0.55 and ~ 0.65 for **M20** and **D20**, respectively. Without the LSS effect, the derived constraints are severely biased by more than 3σ for **M20** and even larger for **D20**. On the other hand, in all the cases, our new model incorporating the LSS effect works excellently with the input values being aligned with the degeneracy direction and well within the 1σ region as shown in blue.

It is known that WL effects depend on Ω_m and σ_8 in a degenerate way, and the derived constraints of the two parameters are highly correlated, as seen from [Fig.8](#) and [Fig.9](#). Such a correlation is often described by a relation $\Sigma_8 = \sigma_8(\Omega_m/0.27)^\alpha$. In [Table.3](#), we list the values of α and Σ_8 for different cases. These values are derived from the principal components analysis of the MCMC samples (for details, please see §4.1 of [Tereno et al. \(2005\)](#) or PCA method in `getdist`⁴). Because [F10](#) model works well for **S10small**, for this case, we also list the values

obtained from the constraints using [F10](#). For the other cases we only show the results derived from the blue regions in [Fig.9](#). We see that for **S10small**, we have $\alpha \approx 0.434$ from [F10](#) and $\alpha \approx 0.452$ from our improved model. The two results are very similar and consistent with the one we obtained from WL peak analyses using CS82 ([X. K. Liu et al. 2015b](#)). For **S20**, **M20** and **D20**, the α value decreases somewhat with the increase of z_{med} . We show their $1 - \sigma$ contours together with the derived degeneracy directions in [Fig.10](#). This indicates the potential of tomographic WL peak analyses, for which, we will explore in detail in our future studies. We also note the α values derived from WL high peak abundances are systematically smaller than those from cosmic shear correlations ([Kilbinger 2015](#)), showing the complementary of the two types of statistical analyses.

3.4. Further tests

The previous analyses show the results with a set of fiducial parameters. In this subsection, we test the validity of the model for different cases. In [Fig.11](#), we show the results with Gaussian smoothing of different smoothing scales with $\theta_G = 1.5$ arcmin (upper), and 3 arcmin (lower), respectively for **S20** in left and **M20** in right. We see the model performs equally well as that of $\theta_G = 2$ arcmin.

In our model, we consider massive halos with $M \geq M_*$ as the dominant sources of high peaks. Simulations show that $M_* \sim 10^{14}h^{-1}\text{M}_\odot$ is an appropriate choice. The very precise value can have dependences on, e.g., the halo mass function and cosmological models. In our fiducial analyses, we take $M_* = 10^{14}h^{-1}\text{M}_\odot$. To test the M_* sensitivity of our model predictions, in [Fig. 12](#), we show the differences of the model predictions with $M_* = 10^{13.9}h^{-1}\text{M}_\odot$ and $10^{14.1}h^{-1}\text{M}_\odot$ with respect to that of the fiducial results. The data points are the differences between the simulation results and the fiducial model predictions with $M_* = 10^{14}h^{-1}\text{M}_\odot$. The large and small error bars are for the survey area of $\sim 150 \text{ deg}^2$ and $\sim 1086 \text{ deg}^2$, respectively. It is seen expectedly that different choice of M_* has no impact on the predicted abundance of very high peaks. For peaks around $\nu_0 \approx 4$ in the considered cases, they show some effects. For surveys of $\sim 150 \text{ deg}^2$ and $z_{\text{med}} = 0.7$, the differences arising from a 0.1dex variation of M_* are within the statistical errors for $\nu_0 \geq 4$. For surveys of $\sim 1000 \text{ deg}^2$, or higher z_{med} , the dependence on M_* becomes significant. We will investigate in more details on this issue in our future studies.

In [Fig.12](#), we extend the horizontal axis to $\nu_0 = 3$. We see that at $\nu_0 \sim 3$, there are some deviations between the model predictions and the simulation results, the higher the z_{med} , the larger the deviations. From [Fig.4](#),

⁴ <http://cosmologist.info/cosmomc>

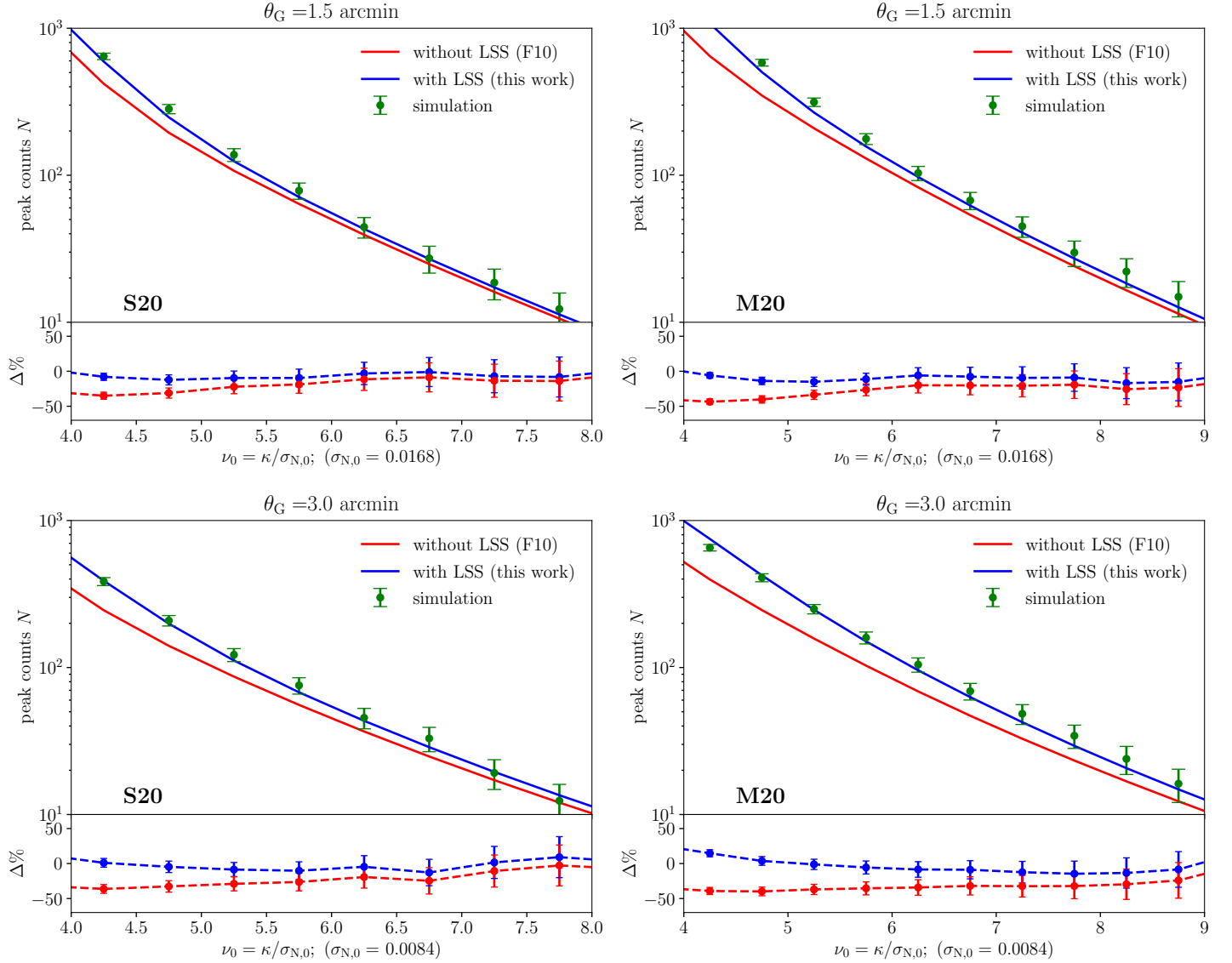


Figure 11. Gaussian smoothing with $\theta_G = 1.5$ arcmin (upper) and $\theta_G = 3.0$ arcmin (lower) for S20 (left) and M20 (right).

we see that in the considered cases, for peaks of $\nu_0 \sim 3$, a significant fraction of them are from the field regions resulting from the combined effects of LSS and shape noise. Thus they are more sensitive to the LSS properties than high peaks that are mainly from halo regions. The Gaussian approximation of the LSS effects needs to be improved to better account for these relatively low peaks, particularly for higher z_{med} where the LSS effects are comparable or even larger than the shape noise effects. This is another important effort in our future studies.

It is noted that our analyses here are done with the convergence fields from simulations directly. On the other hand, observations measure the shape ellipticities of galaxies, which directly give rise to an estimate of the reduced shear $g_i = \gamma_i/(1 - \kappa)$. To perform peak analy-

ses in the convergence fields, in general, we need to first reconstruct them from the shear estimates using the relation between γ and κ . To avoid the reconstructions that may introduce systematic errors, the aperture mass M_{ap} statistics has been proposed with (e.g., [Schneider 1996](#); [Jarvis et al. 2004](#); [van Waerbeke 1998](#)),

$$M_{\text{ap}}(\vec{\theta}) = \int d^2\vec{\theta}' Q(|\vec{\theta} - \vec{\theta}'|) g_t(\vec{\theta}'), \quad (30)$$

where g_t is the tangential component of g with respect to $\vec{\theta} - \vec{\theta}'$. In the regime of $\kappa \ll 1$ and $\vec{g} \approx \vec{\gamma}$, M_{ap} is equal to applying a U filter to the κ field with

$$Q(\theta) = -U(\theta) + \frac{2}{\theta^2} \int \theta' d\theta' U(\theta'). \quad (31)$$

It is required that the U filter is compensated with

$\int d^2\vec{\theta} U(\vec{\theta}) = 0$. Here we present the peak analyses results for M_{ap} obtained by applying an U filter to the simulated convergence fields to show the applicability of our model. We choose a particular filter set with (van Waerbeke 1998; Jarvis et al. 2004):

$$U(\theta, \theta_U) = \frac{1}{\pi\theta_U^2} \left(1 - \frac{\theta^2}{\theta_U^2}\right) \exp\left(-\frac{\theta^2}{\theta_U^2}\right). \quad (32)$$

This filter has smoothed behaviours both in real and in Fourier spaces, and can be handled computationally better than sharply truncated filters (van Waerbeke 1998).

In Fig.3, we already show the comparison of power spectra in Gaussian and in U filters. The U filter can filter out the large-scale contributions more efficiently than that of the Gaussian smoothing. For a visual comparison, we show in Fig.13 the zoom-in maps of the Gaussian and the U filters of a same field. We see that high peaks correspond well in the two cases. On the other hand, large-scale patterns are more apparent in the Gaussian-smoothed map. In Fig.14, we show $\sigma_{\text{LSS},0}/\sigma_{\text{N},0}$ for the two filters for different source redshifts and different smoothing scales. While the LSS effect increases with the source redshift and the smoothing scale in both cases, it is more significant in the Gaussian-filter case than that of the U filter, consistent with the analyses shown in Fig.3 and Fig.13. In Fig.15, we show the signal-to-noise ratio comparison of the corresponding peaks under the two filters. We see that in general, the signal-to-noise ratio is lower in U filter than that in the Gaussian smoothing, which indicates that our peak model can be applicable to lower peaks in the U -filter case. Fig.16 presents the peak number distribution of M_{ap} under the U filter from simulations and also from our model prediction. The results demonstrate that our model works well too in this case, starting from $\nu_0 \approx 2$.

We should note that the equivalence of obtaining M_{ap} from U -filtering of the convergence fields with its original definition is approximate under the assumption of $g \sim \gamma$. For high peaks, however, such an approximation is not accurate enough. Thus to model high aperture-mass peaks better corresponding to real observational analyses, we need to work on the true M_{ap} fields derived directly by applying Q filter to the reduced shear field g_t , which is much more computationally complicated and intensive. Great efforts have been devoted to build such a model and we will present it in our forthcoming paper by Pan et al. (2018).

4. DISCUSSION

In this paper, we analyze the projection effect from stochastic LSS on WL high peak abundances. Similar to F10, we assume that high peaks are dominantly

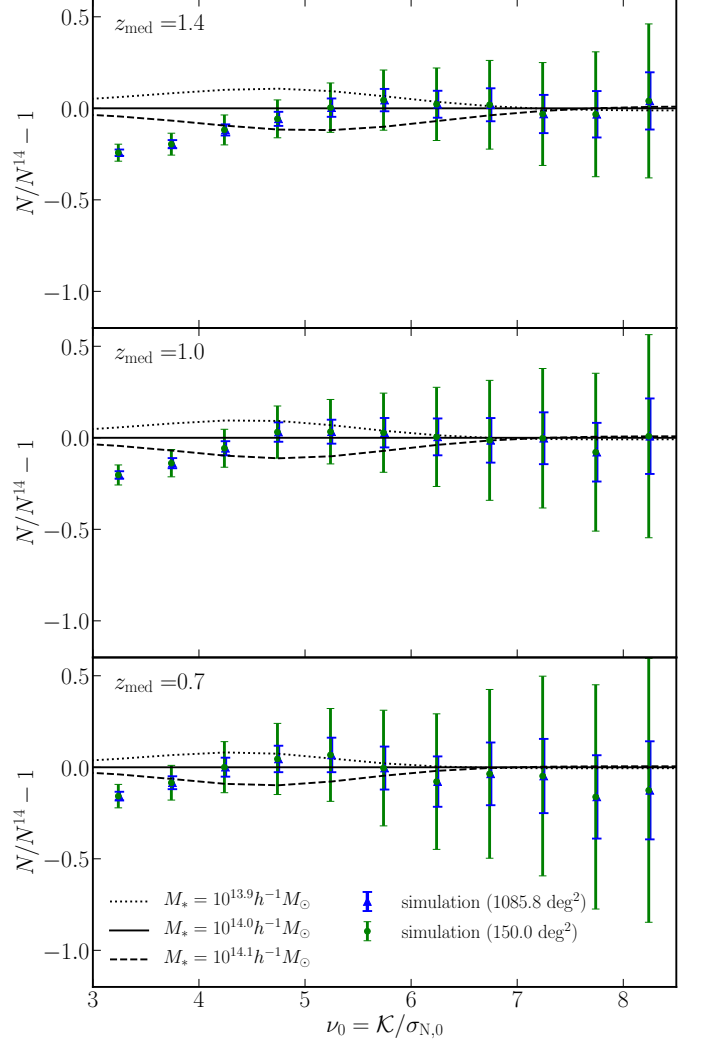


Figure 12. The differences of the model predictions with $M_* = 10^{13.9} h^{-1} M_\odot$ and $M_* = 10^{14.1} h^{-1} M_\odot$ with respect to the fiducial model. The data points are the differences of the simulation results with respect to the fiducial model. The large and small error bars correspond to the survey area of 150 deg^2 and 1086 deg^2 , respectively.

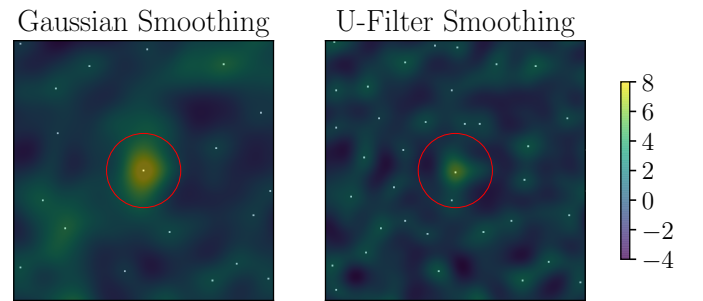


Figure 13. A zoomed-in comparison of convergence maps under Gaussian smoothing (left) and under U filter smoothing (right) of a same field. The smoothing scale is $\theta_G = \theta_U = 2$ arcmin. The color bar for ν_0 in the two cases is shown on the right.

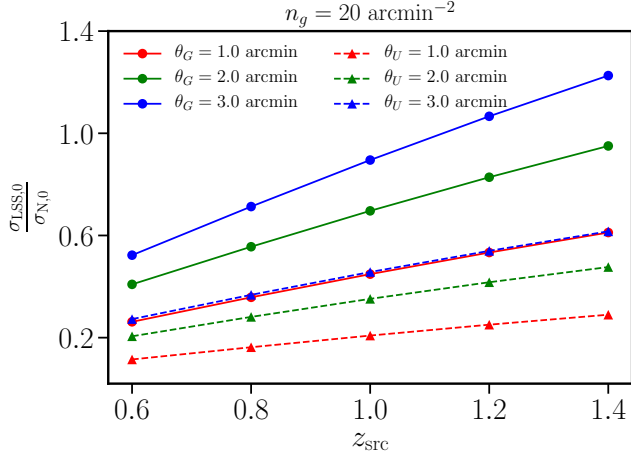


Figure 14. The ratio of $\sigma_{\text{LSS},0}/\sigma_{\text{N},0}$ for Gaussian (solid) and U (dashed) filterings at different source redshifts and different smoothing scales.

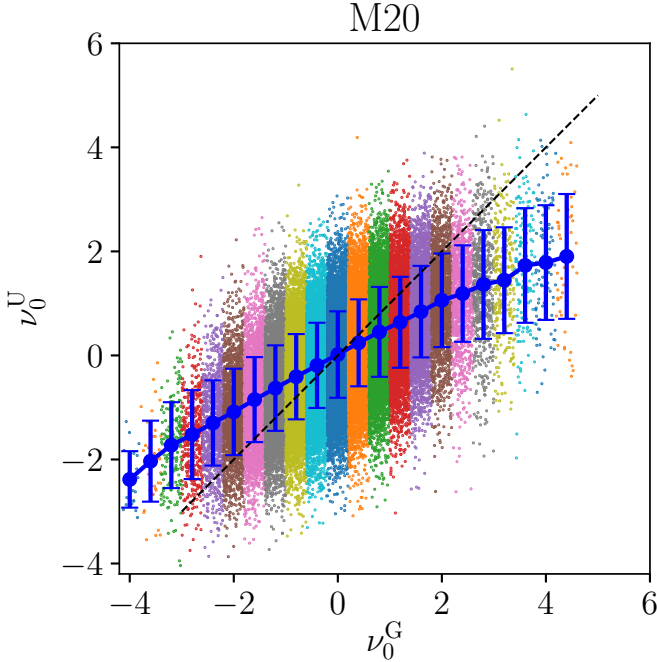


Figure 15. The scatter plot of $\nu_0^G - \nu_0^U$ relation for $\theta_G = \theta_U = 2.0$ arcmin applied to M20 mocks.

from individually massive halos with $M \geq M_*$. To improve F10, we include the LSS effect as a Gaussian random field, and its power spectrum C_ℓ^{LSS} is calculated by subtracting the one-halo contribution from halos with $M \geq M_*$ from the overall non-linear power spectrum. In other words, in our modeling, we treat the heavily non-Gaussian contributions from massive halos to WL peaks separately using their halo mass function and the density profiles. The rest of the line-of-sight projection effect is regarded as the LSS effect modeled as a Gaussian random field. We comment that in line with the

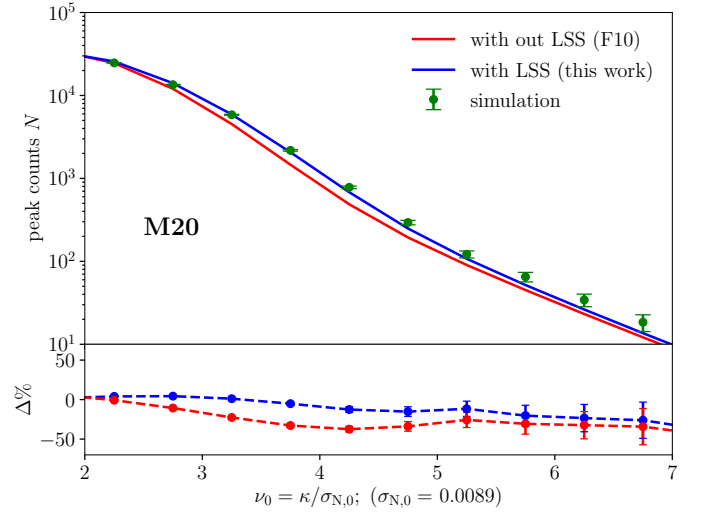
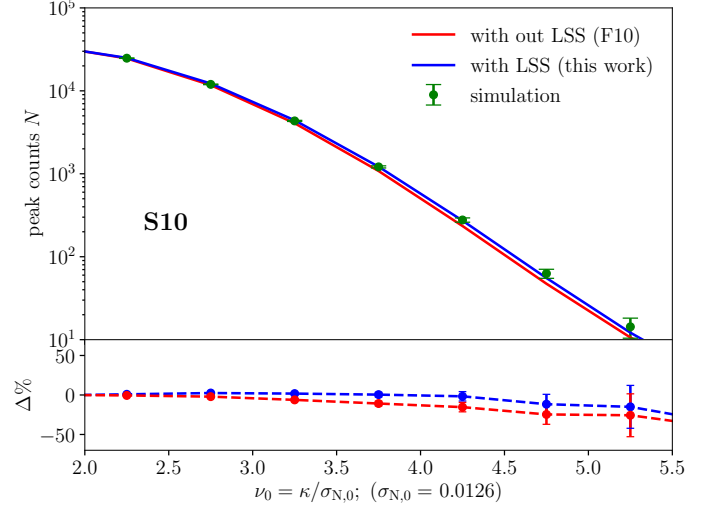


Figure 16. Aperture peak abundance for S10 and M20. The U-filter smoothing scale is $\theta_U = 2.0$ arcmin.

halo model, C_ℓ^{LSS} contains contributions from one-halo terms of smaller halos with $M < M_*$ and the two-halo terms between all the halos. It is also noted the exclusion of the one-halo terms from halos with $M \geq M_*$ is important in calculating C_ℓ^{LSS} correctly. Otherwise, the LSS projection effect would be overestimated.

To exam our model performance, we carry out extensive simulation studies by generating WL maps with respect to different survey conditions. Our analyses show that for a CFHTLenS-like surveys (**S10small**), the LSS effect on WL high peak counts and subsequently the derived cosmological constraints is negligible. This is due to its relatively small contribution to σ_0 in comparison to that of the shape noise and the large statistical errors resulting from a small sky coverage. With the same $n_g = 10 \text{ arcmin}^{-2}$ and $z_{\text{med}} = 0.7$ but increasing the survey area to $\sim 1086 \text{ deg}^2$ (**S10**), the F10 model gives

rise to constraints that are at the edge of 1σ contour. Keeping the same survey depth with $z_{\text{med}} = 0.7$ but increasing n_g to 20 arcmin^{-2} , the LSS projection effect becomes notable. Further increasing the survey depth represented by increasing z_{med} , the LSS projection effect gets more and more important. With the **F10** model without the LSS projection effect, the cosmological constraints derived from WL high peak counts are biased by more than 2σ and 3σ for **S20** and **M20**, and even larger for **D20**. This shows clearly that for future large WL surveys, the LSS projection effect on WL high peaks must be taken into account. Our model presented in this paper performs very well in catching up the effect. We address that in our improved model, C_ℓ^{LSS} contributes additional cosmological information.

We also show the good performance of the model for different smoothing scale θ_G and for the aperture-mass peaks with a compensated U filter. For the latter, we should keep in mind that the true aperture-mass fields are calculated from the reduced shears g rather than from the shears γ .

We note that the mass function and the density profile of halos are important ingredients in our model calculations. Their uncertainties can potentially affect the model predictions. In the analyses here, we take the halo mass function from [Watson et al. \(2013\)](#) and the NFW halo density profile with the mass-concentration relation of [Eq.\(23\)](#). They work well in our comparisons with simulated high peak counts. For future very high precision studies, we need to consider these uncertainties more carefully. Considering the complicated mass distributions in real halos, there should be a negative bias ($\approx 10\%$) in the 2D weak-lensing-derived M - c relation with respect to that of 3D ([Du et al. 2015](#)). As a test, we reduce the A value in the mass-concentration relation by 10%, the theoretical predictions for high peak counts decrease at the level of $\sim 10\%$ for the highest bins in [Fig.7](#), and smaller for lower bins. This is still within the statistical uncertainties of the peak counts in our considered cases here with $\sim 1100 \text{ deg}^2$. With S being $\sim 15,000 \text{ deg}^2$ for future surveys, such as LSST ([LSST Dark Energy Science Collaboration 2012](#)) and Euclid ([Amendola et al. 2013](#)), highly accurate knowledge about these ingredients is needed for precision studies. On the other hand, self-calibrated approaches are possible to constrain, e.g, the mass-concentration rela-

tion, simultaneously with cosmological parameters from WL peak counts ([X. K. Liu et al. 2015b](#)). We will investigate these issues in detail in our future studies.

It is also noted that our model applies to high peaks for which the signals are mainly from single massive halos. On the other hand, simulations have shown that low peaks also contain important cosmological information. It is highly desirable to build theoretical models for them. For low peaks, such as that shown in [Fig.2](#), however, we cannot find a single halo that contributes dominantly to the peak signal. Thus as one of our important future tasks, we need to explore different approaches to model the low/medium peaks.

WL peak analysis has shown its power in cosmological studies. Ongoing and future WL surveys will increase the data in quantity by orders of magnitude comparing to that we currently have. This will lead to a tremendous increase of the statistical power of WL studies. Meanwhile, however, much tighter systematic error controls are needed. Besides the LSS projection effect on WL peaks studied in this paper, there are other systematics that we need to understand carefully, such as the intrinsic alignments of source galaxies, photometric redshift errors, baryonic effects, etc.. Fully exploring the complementarity of WL peak analyses and cosmic shear correlations, not only on cosmological constraints, but also on different responses to systematics, is also an important and exciting direction to work on.

ACKNOWLEDGEMENTS

We thank the referee for very constructive comments and suggestions that help to improve our paper significantly. We are grateful for the discussions with Wei Du and Ran Li. This research is supported in part by the NSFC of China under grants 11333001, 11173001 and by Strategic Priority Research Program *The Emergence of Cosmological Structures* of the Chinese Academy of Sciences, grant No. XDB09000000. X.K.L. acknowledges the support from YNU Grant KC1710708 and General Financial Grant from China Postdoctoral Science Foundation with Grant No. 2016M591006. Q. W. acknowledges the support from NSFC with Grant No. 11403035. We acknowledge the Shuguang cluster at Shanghai Normal University and the High-performance Computing Platform of Peking University for providing computational resources.

REFERENCES

- Albrecht, A., et al. 2006, ArXiv e-prints, astro-ph/0609591
- Amendola, L., et al. 2013, Living Reviews in Relativity, 16, 6
- Bartelmann, M. 1995, A&A, 303, 643
- Bartelmann, M., & Schneider, P. 2001, PhR, 340, 291
- Becker, M. R., et al. 2016, PhRvD, 94, 022002
- Cooray, A., & Sheth, R. 2002, PhR, 372, 1
- Dark Energy Survey Collaboration: Abbott, T., et al. 2016, MNRAS, 460, 1270

- Dietrich, J. P., & Hartlap, J. 2010, MNRAS, 402, 1049
- Du, W., Fan, Z., Shan, H., et al. 2015, ApJ, 814, 120
- Duffy, A. R., Schaye, J., Kay, S. T., & Dalla Vecchia, C. 2008, MNRAS, 390, L64
- Fan, Z. H., Shan, H. Y., & Liu, J. Y. 2010, ApJ, 719, 1408
- Fu, L., et al. 2008, A&A, 479, 9
- Fu, L. P., & Fan, Z. H. 2014, Research in Astronomy and Astrophysics, 14, 1061
- Fu, L. P., et al. 2014, MNRAS, 441, 2725
- Hamana, T., Oguri, M., Shirasaki, M., & Sato, M. 2012, MNRAS, 425, 2287
- Hamana, T., Takada, M., & Yoshida, N. 2004, MNRAS, 350, 893
- Hilbert, S., Hartlap, J., White, S., & Schneider, P. 2009, A&A, 499, 31
- Hildebrandt, H., Viola, M., Heymans, C., et al. 2017, MNRAS, 465, 1454
- Jarvis, M., Bernstein, G., & Jain, B. 2004, MNRAS, 352, 338
- Jee, M. J., Tyson, J. A., Hilbert, S., et al. 2016, ApJ, 824, 77
- Jullo, E., Pires, S., Jauzac, M., & Kneib, J.-P. 2014, MNRAS, 437, 3969
- Kacprzak, T., Kirk, D., Friedrich, O., et al. 2016, MNRAS, 463, 3653
- Kaiser, N. 1993, ApJ, 404, 441
- Kilbinger, M. 2015, Reports on Progress in Physics, 78, 086901
- Kilbinger, M., et al. 2013, MNRAS, 430, 2200
- Kratochvil, J. M., Haiman, Z., & May, M. 2010, PhRvD, 81, 043519
- Lewis, A., Challinor, A., & Lasenby, A. 2000, ApJ, 538, 473
- Lin, C.-A., & Kilbinger, M. 2015, A&A, 576, A24
- Liu, J., & Haiman, Z. 2016, PhRvD, 94, 043533
- Liu, J., Petri, A., Haiman, Z., et al. 2015a, PhRvD, 91, 063507
- Liu, X. K., Wang, Q., Pan, C. Z., & Fan, Z. H. 2014, ApJ, 784, 31
- Liu, X. K., Pan, C. Z., Li, R., et al. 2015b, MNRAS, 450, 2888
- Liu, X. K., Li, B. J., Zhao, G. B., et al. 2016, PhRvL, 117, 051101
- LSST Dark Energy Science Collaboration. 2012, ArXiv e-prints, arXiv:1211.0310
- Marian, L., Smith, R. E., & Bernstein, G. M. 2009, ApJL, 698, L33
- Martinet, N., Schneider, P., Hildebrandt, H., et al. 2018, MNRAS, 474, 712
- Maturi, M., Angrick, C., Pace, F., & Bartelmann, M. 2010, A&A, 519, A23
- Navarro, J. F., Frenk, C. S., & White, S. D. M. 1996, ApJ, 462, 563
- . 1997, ApJ, 490, 493
- Pan, C. Z., Liu, X., Wang, Q., & Fan, Z.-H. 2018, in preparation
- Pen, U., et al. 2003, ApJ, 592, 664
- Schneider, P. 1996, MNRAS, 283, 837
- Seitz, C., & Schneider, P. 1995, A&A, 297, 287
- . 1997, A&A, 318, 687
- Semboloni, E., et al. 2011, MNRAS, 410, 143
- Shan, H., Liu, X., Hildebrandt, H., et al. 2018, MNRAS, 474, 1116
- Shan, H. Y., Kneib, J.-P., Tao, C., et al. 2012, ApJ, 748, 56
- Shan, H. Y., Kneib, J.-P., Comparat, J., et al. 2014, MNRAS, 442, 2534
- Shirasaki, M., Hamana, T., & Yoshida, N. 2015, MNRAS, 453, 3043
- Springel, V. 2005, MNRAS, 364, 1105
- Squires, G., & Kaiser, N. 1996, ApJ, 473, 65
- Takahashi, R., Sato, M., Nishimichi, T., Taruya, A., & Oguri, M. 2012, ApJ, 761, 152
- Tang, J. Y., & Fan, Z. H. 2005, ApJ, 635, 60
- Tereno, I., Doré, O., van Waerbeke, L., & Mellier, Y. 2005, A&A, 429, 383
- van Waerbeke, L. 1998, A&A, 334, 1
- . 2000, MNRAS, 313, 524
- Van Waerbeke, L., et al. 2013, MNRAS, 433, 3373
- Watson, W. A., Iliev, I. T., D'Aloisio, A., et al. 2013, MNRAS, 433, 1230
- Wei, C.-L., Li, G.-L., Kang, X., et al. 2018, MNRAS, submitted
- Weinberg, D. H., Mortonson, M. J., Eisenstein, D. J., et al. 2013, PhR, 530, 87
- White, M., van Waerbeke, L., & Mackey, J. 2002, ApJ, 575, 640
- Yang, X., Kratochvil, J. M., Wang, S., et al. 2011, PhRvD, 84, 043529
- Zorrilla Matilla, J., Haiman, Z., Hsu, D., Gupta, A., & Petri, A. 2016, arXiv:1609.03973